

# Symmetry, Maximally Localized Wannier States, and a Low-Energy Model for Twisted Bilayer Graphene Narrow Bands

Jian Kang<sup>1,\*</sup> and Oskar Vafek<sup>1,2,†</sup>

<sup>1</sup>*National High Magnetic Field Laboratory, Tallahassee, Florida 32304, USA*

<sup>2</sup>*Department of Physics, Florida State University, Tallahassee, Florida 32306, USA*

 (Received 24 May 2018; revised manuscript received 13 July 2018; published 28 September 2018)

We build symmetry-adapted maximally localized Wannier states and construct the low-energy tight-binding model for the four narrow bands of twisted bilayer graphene. We do so when the twist angle is commensurate near the “magic” value and the narrow bands are separated from the rest of the bands by energy gaps. On each layer and sublattice, every Wannier state has three peaks near the triangular moiré lattice sites. However, each Wannier state is localized and centered around a site of the honeycomb lattice that is dual to the triangular moiré lattice. The space group and the time-reversal symmetries are realized locally. The corresponding tight-binding model provides a starting point for studying the correlated many-body phases.

DOI: [10.1103/PhysRevX.8.031088](https://doi.org/10.1103/PhysRevX.8.031088)

Subject Areas: Condensed Matter Physics, Graphene

## I. INTRODUCTION

The discovery of superconductivity and correlated insulator(s) in the “magic” angle twisted bilayer graphene [1,2] has resulted in a remarkable flurry of theoretical activity [3–18]. Central theoretical challenges are to understand the nature and the mechanism of the insulator(s) and the superconductor. Should the most prominent insulating states—which onset at two electrons or holes per triangular moiré unit cell, i.e., at quarter filling of the four narrow bands—be thought of as a largely featureless Mott state in which charge motion is arrested by the Coulomb repulsion, or is a spontaneously broken symmetry responsible for the charge gap? Is the superconductivity unconventional in that it breaks some of the lattice symmetries and perhaps originates from the electron-electron repulsion without a major role from electron-phonon interaction, or is it conventional?

In order to address the above questions, it is necessary to first construct a realistic but simple model of the electron motion in the narrow bands. As pointed out in Refs. [5,6], this is not an obvious task. When the twist angle is commensurate, the moiré pattern becomes periodic and leads to the triangular superlattice; see, e.g., Ref. [19]. At small twist angles, a unit cell contains a large number of carbon atoms, and, consequently, the moiré Brillouin zone (MBZ) becomes small. Indeed, the low-energy band

structure of twisted bilayer graphene (TBG) differs in important aspects from that of two isolated monolayers due to the sizable interlayer tunneling. The four bands around the charge neutrality point have a strongly reduced bandwidth and Fermi velocity. When the twist angle is fine-tuned to the magic values, the bandwidth becomes very narrow (but nonzero), the Fermi velocity at the Dirac cones vanishes, and the quadratic band touching points appear at the corners of the MBZ [1].

Although the local charge density at quarter filling is peaked at the triangular moiré lattice sites [1], as recognized in Refs. [5,6], the salient features of the narrow-band structure cannot be recovered unless the Wannier states (WSs) are centered at the dual honeycomb sites. We prove this using different arguments below. In addition, we diagonalize a microscopic tight-binding model with a large number of atoms in the unit cell according to the prescription by Moon and Koshino [20]. Based on the layer and the microscopic carbon sublattice structure of the resulting Bloch states at the MBZ center, we construct the initial ansatz for the localized WSs which we project onto the Hilbert space spanned by the four narrow bands [21]. By construction, our ansatz realizes the lattice and the time-reversal symmetries locally and forms a *nontrivial* representation of the site symmetry group. The result is then used as the initial step in the iterative procedure of Marzari and Vanderbilt [21] to construct maximally localized, yet symmetry adapted [22], WSs. They, as well as the initial ansatz, are then used to construct and compare the low-energy tight-binding models.

Several theories have been proposed to address the insulating and superconducting phases [3–18]. The closest to ours are Refs. [5,6]. However, there are also important differences. In the theory of Ref. [6], the valley  $U(1)$

\*jian.kang@fsu.edu

†vafek@magnet.fsu.edu

*Published by the American Physical Society under the terms of the Creative Commons Attribution 4.0 International license. Further distribution of this work must maintain attribution to the author(s) and the published article's title, journal citation, and DOI.*

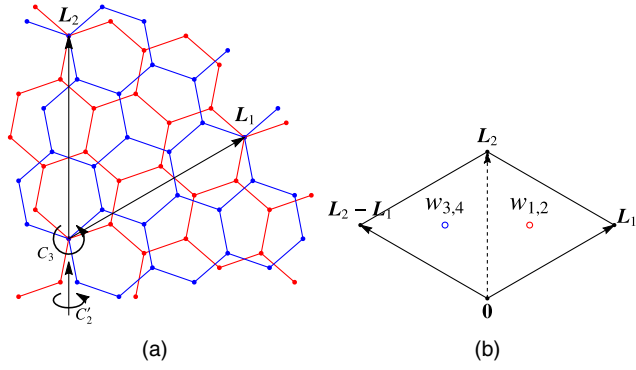


FIG. 1. (a) The superlattice of twisted bilayer graphene. Blue (red) sites are the carbon atoms on the bottom (top) layers. The triangular lattice forms when twist angle is commensurate. The plot shows the lattice when  $m = 2$  and  $n = 1$ . (b) The center of the local Wannier states. Black dots are the sites of the triangular superlattice. Red and blue dots are two nonequivalent Wyckoff sites, where the local Wannier states are centered. In our construction,  $w_1$  and  $w_2$  are placed at one Wyckoff position, and  $w_3$  and  $w_4$  are placed at another position. Note that the Wyckoff sites form an emergent honeycomb lattice.

symmetry and its spontaneous breaking play an important role. Such a valley symmetry, together with the product of  $C_2$  and time reversal, is claimed to be an obstruction to building a tight-binding model for the four narrow bands [6]. In our microscopic construction, we have only the threefold rotation about the axis formed by the AA stacked carbon atoms ( $C_3$ ), the twofold rotation about the axis perpendicular to the two atoms ( $C'_2$ ), and the time-reversal symmetry [see Fig. 1(a)]. We find the same group representations of the Bloch states at the high-symmetry MBZ points as conjectured in Ref. [5]. Although the WSs were not constructed explicitly in Ref. [5], the WS symmetry was insightfully deduced and is in agreement with our findings. The three-peak structure of the WSs, which we find explicitly [see Fig. 3(c)], was also recognized in Ref. [6] and dubbed “fidget spinner.”

## II. SUPERLATTICE AND BAND STRUCTURE OF THE TBG

For a commensurate twist angle, the moiré pattern can be specified by two integers  $(m, n)$ ; see, e.g., Ref. [19]. The primitive translation vectors are  $L_1 = ma_1 + na_2 = nb_1 + mb_2$  and  $L_2 = -na_1 + (m+n)a_2 = -mb_1 + (m+n)b_2$ , where  $a_1$  and  $a_2$  ( $b_1$  and  $b_2$ ) are the primitive vectors of the top (bottom) layer graphene lattice. As shown in Fig. 1, the triangular superlattice sites are the positions of AA stacking. The point group symmetry operations form the  $D_3$  group generated by  $C_3$  and  $C'_2$ , leading to nontrivial symmetry representations of the Bloch states at the high-symmetry points in MBZ, especially at  $\Gamma$  ( $k = 0$ ) and  $K$  ( $k = [(4\pi)/(3L_1^2)]L_1$ ).

We calculate the band structure based the microscopic model of Ref. [20], which gives the values of the intralayer and the interlayer carbon-carbon tunneling amplitudes. Their tight-binding Hamiltonian is written as

$$H = - \sum_{r_i, r_j} t(r_i - r_j) c_{r_i}^\dagger c_{r_j} \quad \text{with}$$

$$t(d) = -V_{pp\pi} \left[ 1 - \left( \frac{d \cdot e_z}{d} \right)^2 \right] - V_{pp\sigma} \left( \frac{d \cdot e_z}{d} \right)^2,$$

$$V_{pp\pi} = V_{pp\pi}^0 \exp \left( -\frac{d - a_0}{\delta} \right),$$

$$V_{pp\sigma} = V_{pp\sigma}^0 \exp \left( -\frac{d - d_0}{\delta} \right), \quad (1)$$

where  $c_{r_i}$  and  $c_{r_i}^\dagger$  are the annihilation and creation operators of the electron at the carbon site  $r_i$ . We set  $V_{pp\pi}^0 = -2.7$  eV,  $V_{pp\sigma}^0 = 0.48$  eV.  $a_0 = 0.142$  nm is the distance between the two nearest-neighbor carbon atoms on the same layer;  $d_0 = 0.335$  nm is the interlayer distance. The decay length for the hopping is  $\delta = 0.319a_0$ . The hopping with  $d > 4a_0$  is exponentially small and, thus, is neglected in the model. All these detailed parameters are reproduced from Ref. [20] and listed here for completeness. The MBZ contains three high-symmetry points  $\Gamma$ ,  $K$ , and  $K'$ . The time-reversal symmetry (TRS) transforms  $K$  and  $K'$  into each other and leaves  $\Gamma$  invariant.

As illustrated in Fig. 2, this model contains four narrow bands with very small bandwidths near the charge neutrality point where the zero of energy is defined. Depending on the value of the twist angle, these four bands may or may not be separated by an energy gap from the other bands in the spectrum. When  $m - n = \pm 1 \bmod 3$  [19] at the  $K$  point, two bands form a Dirac cone, and the remaining two bands are split by a tiny gap ( $< 0.01$  meV). These four Bloch states at  $K$  form a two-dimensional representation ( $E$ ) and two one-dimensional representations ( $A_1$  and  $A_2$ ) of the group  $D_3$  [5],

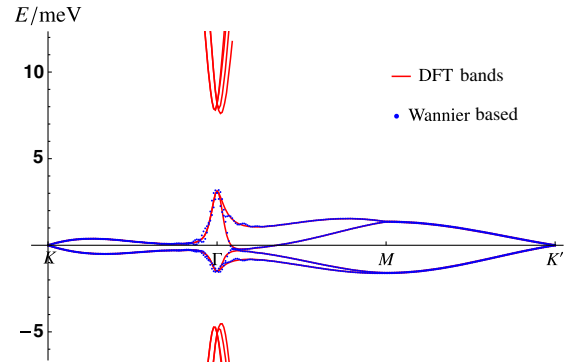


FIG. 2. Red dots: The four narrow bands produced from the tight-binding model with hopping parameters given in Ref. [20] with the twist angle of  $1.30^\circ$ . Blue dots: The interpolated band structure by the projection method.

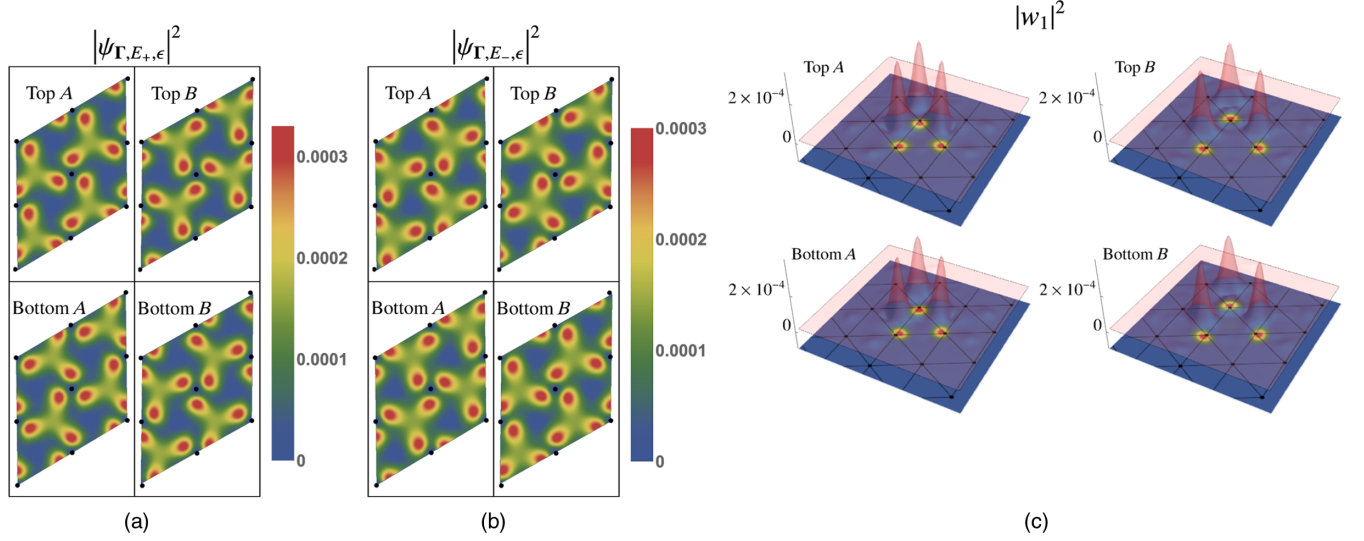


FIG. 3. (a),(b) The square of the magnitude of the Bloch states  $|\psi_{\Gamma,E\pm,\epsilon}|^2$  and  $|\psi_{\Gamma,E-,\epsilon}|^2$  and (c) the localization of the WSs obtained from the projected method. The four panels show  $|w_i|^2$  at (upper left) the top layer sublattice A, (upper right) the top layer sublattice B, (lower left) the bottom layer sublattice A, and (lower right) the bottom layer sublattice B.

consistent with the degeneracy described above. The Bloch states at the center of the MBZ  $\Gamma$  are doubly degenerate; the energy difference between the two pairs defines the (narrow) bandwidth. The doublets are the two-dimensional representations ( $E$ ) of the group  $D_3$  [5]. Using  $\epsilon$  to represent the phase factor  $\epsilon = \exp(i2\pi/3)$  [23], we choose the two components of each doublet to transform as the eigenstates of  $C_3$  with the eigenvalues of either  $\epsilon$  or  $\epsilon^*$ , and label the four Bloch states at  $\Gamma$  as  $\psi_{\Gamma,E\pm,\epsilon^{\pm 1}}$ . Here,  $E_{\pm}$  refers to the doublet with higher (lower) energy, and  $\epsilon^{\pm 1}$  refers to the component of the doublet which has the eigenvalue of  $\epsilon$  ( $\epsilon^*$ ) under  $C_3$ . While the two components of each doublet are the eigenstates of  $C_3$ , they transform into each other under  $C_2'$  and the TRS. We wish to stress that there is no simple transformation which relates the two doublets at different energy, i.e.,  $\psi_{\Gamma,E_{\pm}}$ . This fact can be seen in Figs. 3(a) and 3(b) where  $|\psi_{\Gamma}|^2$  are plotted.

### III. WANNIER STATES

Our next step is to construct the localized WSs by applying the projection method [21]. For this purpose, it is necessary that the four bands are separated by a gap from all others. The experiments of Refs. [1,2] determined that the closest simple commensurate values are  $m = 30$  and  $n = 31$ . However, the four bands produced by Eq. (1) are gapped only near the band maximum, not near the band minimum; this is also seen in Ref. [1] Fig. 1. Such a connection with the bands below contradicts the experimental finding that the four bands of interest are separated from either side by insulating states [1]. Therefore, we construct the WSs for the case of  $m = 25$  and  $n = 26$  (with the twist angle  $\theta = 1.30^\circ$ ); the four bands are then separated by a gap on both sides. We expect that the values of the hopping parameters of the low-energy Hamiltonian at the

magic angle to be almost the same, and, importantly, can be fine-tuned to it by slight modification. We confirm that the quadratic band touching at  $\mathbf{K}$ , which can be taken to be the defining property of the magic angle, can be realized in such a way.

#### A. Symmetry of the Wannier states

As mentioned, it is crucial to identify the positions of the WSs. One naive choice is to place centers of all four states on the triangular moiré superlattice sites. With this option, the WSs transform as

$$g|w_{i,\mathbf{R}}\rangle = \sum_j |w_{j,g\mathbf{R}}\rangle U_{ji}(g), \quad (2)$$

where  $i, j = 1, \dots, 4$  are the indices of the WSs,  $\mathbf{R}$  is the position of the triangular superlattice site, and  $g$  is the symmetry operation. The Bloch state  $\psi_{i,\mathbf{k}}$  is the linear superposition of the WSs. Under the same symmetry operation  $g$ , we find

$$\begin{aligned} g|\psi_{i,\mathbf{k}}\rangle &= g \sum_{\mathbf{R}} e^{i\mathbf{k}\cdot\mathbf{R}} |w_{i,\mathbf{R}}\rangle = \sum_{\mathbf{R}} e^{i\mathbf{k}\cdot\mathbf{R}} |w_{j,g\mathbf{R}}\rangle U_{ji}(g) \\ &= \sum_{\mathbf{R}} e^{i\mathbf{gk}\cdot\mathbf{gR}} |w_{j,g\mathbf{R}}\rangle U_{ji}(g) = |\psi_{j,\mathbf{gk}}\rangle U_{ji}(g). \end{aligned} \quad (3)$$

It is interesting to study the special case when the momentum is symmetry invariant, i.e.,  $\Gamma$  and  $\mathbf{K}$  in the MBZ. We immediately conclude that the Bloch states should transform as  $U(g)$ , and, therefore, the Bloch states should transform in the *same* way at  $\Gamma$  and  $\mathbf{K}$ . As we point out, the four Bloch states transform as two doublets at  $\Gamma$  and one doublet and two singlets at  $\mathbf{K}$ . This proves that the



symmetry of the Bloch states cannot be reproduced if all the WSs are placed at the sites of the triangular superlattice.

The argument above suggests that the centers of the four WSs should be placed at nonequivalent sites (Wyckoff positions) to reproduce the symmetry representations at  $\Gamma$  and  $K$ . A better choice is to place them at the centers of the equilateral triangles [Fig. 1(b)], which form the dual honeycomb lattice [5,6]. Note that each triangular superlattice unit cell contains two honeycomb lattice sites. The two WSs  $w_1$  and  $w_2$  should be placed at one site and  $w_3$  and  $w_4$  at another site.

To illustrate the symmetry of the Wannier states, we start by modifying Eq. (2) for the dual honeycomb lattice [22],

$$g|w_{i,\mathbf{R}}\rangle = \sum_j |w_{j,g\mathbf{R}+\mathbf{R}'(g,i)}\rangle U_{ji}(g), \quad (4)$$

where  $\mathbf{R}$  and  $\mathbf{R}'$  are still the *triangular* lattice translation vectors, and the latter vector depends only on  $g$  and the WS index  $i$ . Equation (3) now takes the form [22]

$$g|\psi_{i,\mathbf{k}}\rangle = |\psi_{j,g\mathbf{k}}\rangle e^{-ig\mathbf{k}\cdot\mathbf{R}'} U_{ji}(g). \quad (5)$$

Note that the extra phase factor  $e^{-ig\mathbf{k}\cdot\mathbf{R}'}$  now differentiates between  $\Gamma$  (where it is 1) and  $K$  (in general, nontrivial). For  $g = C_3$  and  $\mathbf{k} = \Gamma$ , the matrix  $U$  must be diagonal; i.e., all four WSs must be eigenstates of the  $C_3$  followed by a lattice translation with the same eigenvalues as those of  $|\psi_{i,\Gamma}\rangle$ . We therefore choose  $w_{1,4}$  and  $w_{2,3}$  to have the eigenvalues  $\epsilon$  and  $\epsilon^*$ , respectively. Next, because  $C'_2$  interchanges the two nonequivalent Wyckoff positions and the  $C_3$  eigenvalues, we can set  $C'_2 w_1 = w_3$  and  $C'_2 w_2 = w_4$ ; see Fig. 1(b). Finally, the time-reversal symmetry does not change the position of the WSs, but it does conjugate the eigenvalue of  $C_3$ . Therefore,  $\mathcal{T} w_1 = w_2$  and  $\mathcal{T} w_3 = w_4$ . These transformation rules together with translation symmetry enforce the symmetry of any low-energy model.

## B. Projection method

In this subsection, we explain the projection method we use to produce the localized WSs as the input of the WANNIER90 program. We follow the approach in Ref. [21]. As explained in the text, we first construct the trial functions  $|h_i\rangle$  ( $i = 1, \dots, 4$ ), which transform in the same way as the WSs. These trial states are not necessarily orthogonal or normalized. For the Bloch states  $|\psi_{i,\mathbf{k}}\rangle$ , we define the matrix  $A(\mathbf{k})_{ij} = \langle \psi_{i,\mathbf{k}} | h_j \rangle$ . The states

$$|\phi_{i,\mathbf{k}}\rangle = \sum_j |\psi_{j,\mathbf{k}}\rangle \langle \psi_{j,\mathbf{k}} | h_i \rangle = \sum_j |\psi_{j,\mathbf{k}}\rangle A_{ji}(\mathbf{k})$$

are smooth in  $\mathbf{k}$  as long as the matrix  $A$  is nonsingular because the arbitrary  $\mathbf{k}$ -dependent phase cancels in the projector. Smoothness in  $\mathbf{k}$  is required in order for WSs to be localized in real space. However, they are not orthonormal. To construct the orthonormalized  $\mathbf{k}$ -smooth

Bloch-like states, we define the matrix  $S(\mathbf{k}) = A^\dagger(\mathbf{k})A(\mathbf{k})$  and

$$|\tilde{\psi}_{i,\mathbf{k}}\rangle = \sum_j |\phi_{j,\mathbf{k}}\rangle S_{ji}^{-1/2}(\mathbf{k}) = \sum_j |\psi_{j,\mathbf{k}}\rangle [A(\mathbf{k})S^{-1/2}(\mathbf{k})]_{ji}.$$

In practice, we apply the singular value decomposition to the matrix  $A(\mathbf{k}) = U(\mathbf{k})D(\mathbf{k})V^\dagger(\mathbf{k})$ , where the matrices  $U(\mathbf{k})$  and  $V(\mathbf{k})$  are unitary, and  $D(\mathbf{k})$  is diagonal. It is easy to show that  $A(\mathbf{k})S^{-1/2}(\mathbf{k}) = U(\mathbf{k})V^\dagger(\mathbf{k})$  is unitary and, thus,  $|\tilde{\psi}\rangle$  is orthogonal and normalized. With the projection method, the WSs are

$$|w_{i,\mathbf{R}}\rangle = \int \frac{d^d \mathbf{k}}{(2\pi)^d} |\tilde{\psi}_{i,\mathbf{k}}\rangle e^{-i\mathbf{k}\cdot\mathbf{R}}.$$

With this method, the Bloch states  $|\tilde{\psi}_{i,\mathbf{k}}\rangle$  constructed from the WSs  $|w_{i,\mathbf{R}}\rangle$  differ from the Bloch states  $|\psi_{i,\mathbf{k}}\rangle$  only by a unitary transformation and, therefore, faithfully reproduce the Hilbert space spanned by  $|\psi_{i,\mathbf{k}}\rangle$ .

It is crucial to choose the appropriate initial trial states as an input of the projection method. As shown in Figs. 3(a) and 3(b), we find that the magnitudes of the Bloch states at  $\Gamma$  display a smooth structure in real space when separated out by the layer and the microscopic carbon sublattice. This observation, along with the above considerations, suggests that a good initial ansatz for  $w_1$  can be constructed as follows: First imagine placing a Gaussian-like cutoff centered at the first dual honeycomb site on  $\psi_{\Gamma,E_+, \epsilon}$  but only on the top layer and sublattice  $A$  and the bottom layer and sublattice  $B$ . The amplitudes at the top layer and the sublattice  $B$  and the bottom layer and the sublattice  $A$  are taken from the similarly cut off  $\psi_{\Gamma,E_-, \epsilon}$ . This choice guarantees good overlap with the Bloch states.  $C'_2$  now generates  $w_3$ , and the TRS generates  $w_2$ ; when the TRS is applied to  $w_3$ , it finally gives  $w_4$ . In addition to the symmetry considerations, our initial trial states are chosen in this way to obtain a good overlap with all four Bloch states  $\Psi_\Gamma$ .

Figure 3(c) shows the shape of the resulting  $|w_1|^2$  on different layers and different sublattices. As seen,  $w_1$  is well localized and centered around the dual honeycomb lattice site; it also displays three different peaks located around the triangular lattice sites. This shape is consistent with the local density of states obtained by density-functional-theory (DFT) calculations which is also peaked around the triangular lattice sites. We checked that the remaining WSs obtained in this way are related by the mentioned symmetry:  $w_2 = w_1^*$ ,  $w_3 = C'_2 w_1$ , and  $w_4 = w_3^*$ . Fourier transformation is done on the WSs to explore the valley distribution of each WS. We find that more than 90% of the WSs  $w_1$  and  $w_4$  are contributed by the electron states around the valley  $K_t$  ( $K_b$ ), where  $K_t = [(4\pi)/(3|a_1|^2)]a_1$  and  $K_b = [(4\pi)/(3|b_1|^2)]b_1$ . Because of the time-reversal symmetry, the same percentage of the WSs  $w_2$  and  $w_3$  are from the electron states around the opposite valley,  $-K_t$  and

$-\mathbf{K}_b$ . This suggests that the two valleys are almost separated in the WSs obtained from the projection method.

In the next step, we use the initial ansatz as an input to the WANNIER90 program [24] with site symmetry enforced on the  $30 \times 30 \mathbf{k}$ -space mesh, and after 200 iterations, we obtain the four maximally localized WSs. Compared with the WSs before WANNIER90, the localization improves by about 20%. However, we find the two valleys are significantly mixed in each WS. In the next section, we compare the hopping amplitudes for these two sets of WSs to illustrate the impact of the approximate valley  $U(1)$  symmetry.

#### IV. TIGHT-BINDING MODEL

In this section, we construct a minimal tight-binding model for the localized WSs. The structure of WSs seen in Fig. 3(c) suggests that the overlap of the next and even the next-next-nearest-neighboring WSs is sizable and, thus, cannot be neglected even in the minimal model. We first derive the most general form of the tight-binding model up to the next-next-nearest-neighbor hopping, and then we calculate the values of the hopping constants for two sets of the WSs: the one obtained from the projection method and the maximally localized WSs obtained from the WANNIER90 program.

##### A. Symmetry constraints

The tight-binding model based on the localized WSs can be readily constructed. In this subsection, we discuss the most general form of the hopping amplitudes allowed by symmetry. The on-site term must be of the form

$$H_{\text{on site}} = -\mu \sum_{\mathbf{R}} \sum_{j=1}^4 f_{j,\mathbf{R}}^\dagger f_{j,\mathbf{R}}, \quad (6)$$

where  $f_{i,\mathbf{R}}^\dagger$  and  $f_{i,\mathbf{R}}$  are the creation and annihilation operators of the WSs  $w_{i,\mathbf{R}}$ . This form of the on-site term is guaranteed because  $C_3$  prohibits mixing between  $w_1$  and  $w_2$ , and  $w_3$  and  $w_4$ ;  $C'_2$  and TRS then force a single real parameter  $\mu$ . In contrast, there are two such parameters in Ref. [6].

The next term is the nearest-neighbor hopping between  $w_{1,2;\mathbf{R}_i}$  and the neighboring  $w_{3,4;\mathbf{R}_j}$ . Thus, the Hamiltonian is of the form

$$H_n = \sum_{\mathbf{R}} \sum_{\substack{i=1,2 \\ j=3,4}} f_{i,\mathbf{R}}^\dagger (t_{ij}^n f_{j,\mathbf{R}} + t_{ij}^{n'} f_{j,\mathbf{R}+\mathbf{L}_1-\mathbf{L}_2} + t_{ij}^{n''} f_{j,\mathbf{R}+\mathbf{L}_1}) + \text{H.c.} \quad (7)$$

It should be invariant under all the symmetry transformations. First, consider  $C_3$ , which brings WSs  $w_{\mathbf{R}}$  into  $w_{\mathbf{R}'}$  in a different unit cell. In addition,  $w_1$  and  $w_4$  have the eigenvalue of  $\epsilon$ , and  $w_2$  and  $w_3$  have the eigenvalue of  $\epsilon^*$ . The  $C_3$  invariance of the Hamiltonian forces

$$t_{14}^n = t_{14}^{n'} = t_{14}^{n''}, \quad t_{23}^n = t_{23}^{n'} = t_{23}^{n''}, \quad (8)$$

$$t_{13}^n = \epsilon t_{13}^{n'} = \epsilon^* t_{13}^{n''}, \quad t_{24}^n = \epsilon^* t_{24}^{n'} = \epsilon t_{24}^{n''}. \quad (9)$$

$C'_2$  transforms  $w_1 \leftrightarrow w_3$  and  $w_2 \leftrightarrow w_4$ , and brings  $\mathbf{L}_1 \rightarrow \mathbf{L}_2 - \mathbf{L}_1$ , and  $\mathbf{L}_2 \rightarrow \mathbf{L}_2$ . Combined with the Hermiticity of the Hamiltonian, the  $C'_2$  invariance leads to  $t_{14}^n = (t_{23}^n)^*$ ,  $t_{13}^n = (t_{13}^n)^*$ , and  $t_{24}^n = (t_{24}^n)^*$ . Finally, the TRS enforces  $t_{13}^n = (t_{24}^n)^*$ .

Combining all constraints, we set  $t_{13}^n = t_1$  and  $t_{14}^n = t'_1$ , where  $t_1$  is real and  $t'_1$  is, in general, a complex number. Thus, the nearest-neighbor hopping term can be written as

$$H_n = \sum_{\mathbf{R}} \begin{pmatrix} f_{1,\mathbf{R}} \\ f_{2,\mathbf{R}} \end{pmatrix}^\dagger \left\{ \begin{pmatrix} t_1 & t'_1 \\ (t'_1)^* & t_1 \end{pmatrix} \begin{pmatrix} f_{3,\mathbf{R}} \\ f_{4,\mathbf{R}} \end{pmatrix} + \begin{pmatrix} \epsilon^* t_1 & t'_1 \\ (t'_1)^* & \epsilon t_1 \end{pmatrix} \begin{pmatrix} f_{3,\mathbf{R}+\mathbf{L}_1-\mathbf{L}_2} \\ f_{4,\mathbf{R}+\mathbf{L}_1-\mathbf{L}_2} \end{pmatrix} + \begin{pmatrix} \epsilon t_1 & t'_1 \\ (t'_1)^* & \epsilon^* t_1 \end{pmatrix} \begin{pmatrix} f_{3,\mathbf{R}+\mathbf{L}_1} \\ f_{4,\mathbf{R}+\mathbf{L}_1} \end{pmatrix} \right\} + \text{H.c.} \quad (10)$$

It seems that  $t'_1$  is a complex number. If we apply a gauge transformation  $w_{1,3} \rightarrow e^{i\theta} w_{1,3}$  and  $w_{2,4} \rightarrow e^{-i\theta} w_{2,4}$ , the hopping constant  $t_1$  is invariant but  $t'_1 \rightarrow e^{2i\theta} t'_1$ . Thus, the phase of  $t'_1$  can be always removed by choosing a particular gauge of the WSs. Therefore, there are only two free parameters for the nearest-neighbor hopping [5].

Next, consider the next-nearest-neighbor hopping  $H_{\text{NN}}$ :

$$H_{\text{NN}} = \sum_{\mathbf{R}} \left( \sum_{i,j=1}^2 + \sum_{i,j=3}^4 \right) f_{i,\mathbf{R}}^\dagger (t_{ij}^{\text{NN},1} f_{j,\mathbf{R}+\mathbf{L}_1} + t_{ij}^{\text{NN},2} f_{j,\mathbf{R}+\mathbf{L}_2-\mathbf{L}_1} + t_{ij}^{\text{NN},3} f_{j,\mathbf{R}-\mathbf{L}_2}) + \text{H.c.} \quad (11)$$

Let us first consider the symmetry constraints on  $t_{ij}^{\text{NN}}$  when  $i, j = 1, 2$ . The  $C_3$  invariance enforces

$$t_{11}^{\text{NN},1} = t_{11}^{\text{NN},2} = t_{11}^{\text{NN},3}, \quad t_{22}^{\text{NN},1} = t_{22}^{\text{NN},2} = t_{22}^{\text{NN},3}, \quad (12)$$

$$t_{12}^{\text{NN},1} = \epsilon t_{12}^{\text{NN},2} = \epsilon^* t_{12}^{\text{NN},3}, \quad t_{21}^{\text{NN},1} = \epsilon^* t_{21}^{\text{NN},2} = \epsilon t_{21}^{\text{NN},3}. \quad (13)$$

The TRS leads to

$$t_{22}^{\text{NN},1} = (t_{11}^{\text{NN},1})^*, \quad t_{21}^{\text{NN},1} = (t_{12}^{\text{NN},1})^*.$$

The hopping constants  $t_{ij}^{\text{NN}}$  ( $i, j = 3$  or  $4$ ) can be obtained by applying  $C'_2$  symmetry operation. Therefore, the next-nearest-neighbor hopping can be described by two complex numbers  $t_2 = t_{11}^{\text{NN},1}$  and  $t'_2 = t_{12}^{\text{NN},1}$ . The general form is

$$\begin{aligned}
H_{\text{NN}} = \sum_{\mathbf{R}} \left( \begin{matrix} f_{1,\mathbf{R}} \\ f_{2,\mathbf{R}} \end{matrix} \right)^\dagger \left\{ \begin{pmatrix} t_2 & t'_2 \\ (t'_2)^* & t_2^* \end{pmatrix} \begin{pmatrix} f_{1,\mathbf{R}+L_1} \\ f_{2,\mathbf{R}+L_1} \end{pmatrix} + \begin{pmatrix} t_2 & \epsilon^* t'_2 \\ \epsilon (t'_2)^* & t_2^* \end{pmatrix} \begin{pmatrix} f_{1,\mathbf{R}+L_2-L_1} \\ f_{2,\mathbf{R}+L_2-L_1} \end{pmatrix} + \begin{pmatrix} t_2 & \epsilon t'_2 \\ \epsilon^* (t'_2)^* & t_2^* \end{pmatrix} \begin{pmatrix} f_{1,\mathbf{R}-L_2} \\ f_{2,\mathbf{R}-L_2} \end{pmatrix} \right\} \\
+ \left( \begin{matrix} f_{3,\mathbf{R}} \\ f_{4,\mathbf{R}} \end{matrix} \right)^\dagger \left\{ \begin{pmatrix} t_2 & t'_2 \\ (t'_2)^* & t_2^* \end{pmatrix} \begin{pmatrix} f_{3,\mathbf{R}+L_2-L_1} \\ f_{4,\mathbf{R}+L_2-L_1} \end{pmatrix} + \begin{pmatrix} t_2 & \epsilon^* t'_2 \\ \epsilon (t'_2)^* & t_2^* \end{pmatrix} \begin{pmatrix} f_{3,\mathbf{R}+L_1} \\ f_{4,\mathbf{R}+L_1} \end{pmatrix} + \begin{pmatrix} t_2 & \epsilon t'_2 \\ \epsilon^* (t'_2)^* & t_2^* \end{pmatrix} \begin{pmatrix} f_{3,\mathbf{R}-L_2} \\ f_{4,\mathbf{R}-L_2} \end{pmatrix} \right\} + \text{H.c.}
\end{aligned} \quad (14)$$

Finally, we consider the symmetry constraints on the next-next-nearest-neighbor hopping with the most general form of

$$\begin{aligned}
H_{\text{NNN}} = \sum_{\mathbf{R}} \sum_{\substack{i=1,2 \\ j=3,4}} f_{i,\mathbf{R}}^\dagger (t_{ij}^{\text{NNN},1} f_{j,\mathbf{R}+2L_1-L_2} + t_{ij}^{\text{NNN},2} f_{j,\mathbf{R}+L_2} \\
+ t_{ij}^{\text{NNN},3} f_{j,\mathbf{R}-L_2}) + \text{H.c.}
\end{aligned} \quad (15)$$

The constraints are very similar to the one for the nearest-neighbor hopping. We find  $C_3$  enforces

$$\begin{aligned}
t_{14}^{\text{NNN},1} = t_{14}^{\text{NNN},2} = t_{14}^{\text{NNN},3}, \quad t_{23}^{\text{NNN},1} = t_{23}^{\text{NNN},2} = t_{23}^{\text{NNN},3}, \\
t_{13}^{\text{NNN},1} = \epsilon t_{13}^{\text{NNN},2} = \epsilon^* t_{13}^{\text{NNN},3}, \quad t_{24}^{\text{NNN},1} = \epsilon^* t_{24}^{\text{NNN},2} = \epsilon t_{24}^{\text{NNN},3}.
\end{aligned}$$

Combined with the Hermiticity of the Hamiltonian,  $C_2'$  leads to

$$t_{13}^{\text{NNN},1} = (t_{13}^{\text{NNN},1})^*, \quad t_{24}^{\text{NNN},1} = (t_{24}^{\text{NNN},1})^*, \quad t_{14}^{\text{NNN},1} = (t_{23}^{\text{NNN},1})^*.$$

The TRS puts an additional constraint  $t_{13}^{\text{NNN},1} = (t_{24}^{\text{NNN},1})^*$ . Thus, we can introduce one real  $t_3 = t_{13}^{\text{NNN},1}$  and one

complex  $t'_3 = t_{14}^{\text{NNN},1}$  parameter for the next-next-nearest-neighbor hopping. The Hamiltonian takes the form

$$\begin{aligned}
H_{\text{NNN}} = \sum_{\mathbf{R}} \left( \begin{matrix} f_{1,\mathbf{R}} \\ f_{2,\mathbf{R}} \end{matrix} \right)^\dagger \left\{ \begin{pmatrix} t_3 & t'_3 \\ (t'_3)^* & t_3 \end{pmatrix} \begin{pmatrix} f_{3,\mathbf{R}+2L_1-L_2} \\ f_{4,\mathbf{R}+2L_1-L_2} \end{pmatrix} \right. \\
+ \begin{pmatrix} \epsilon^* t_3 & t'_3 \\ (t'_3)^* & \epsilon t_3 \end{pmatrix} \begin{pmatrix} f_{3,\mathbf{R}+L_2} \\ f_{4,\mathbf{R}+L_2} \end{pmatrix} \\
\left. + \begin{pmatrix} \epsilon t_3 & t'_3 \\ (t'_3)^* & \epsilon^* t_3 \end{pmatrix} \begin{pmatrix} f_{3,\mathbf{R}-L_2} \\ f_{4,\mathbf{R}-L_2} \end{pmatrix} \right\} + \text{H.c.}
\end{aligned} \quad (16)$$

The symmetry constraints on further range hopping can be worked out in the same way.

## B. Values of the hopping constants

The most general tight-binding Hamiltonian is of the form

$$H = \sum_{\mathbf{R}, \mathbf{r}} \sum_{i,j=1}^4 t_{ij,\mathbf{r}} f_{i,\mathbf{R}}^\dagger f_{j,\mathbf{R}+\mathbf{r}}, \quad (17)$$

where both  $\mathbf{R}$  and  $\mathbf{r}$  are the triangular lattice vectors. The hopping constants  $t$  are indexed by two WS indices  $i$  and  $j$ ,

TABLE I. The hopping constants between  $w_{1,2}$  and  $w_{3,4}$ . The number outside (inside) the parentheses is for WSs obtained from the projection method (WANNIER90). All the numbers are in units of milli-electron volts.

$t_{13,0} = \epsilon t_{13,(1,-1)} = \epsilon^* t_{13,(1,0)}$	-0.011 (0.0831)
$t_{14,0} = t_{14,(1,0)} = t_{14,(1,-1)}$	0.0177 + 0.2910i (0.0380 + 0.2603i)
$t_{13,(2,-1)} = \epsilon t_{13,(0,1)} = \epsilon^* t_{13,(0,-1)}$	-0.0006 (-0.0853)
$t_{14,(2,-1)} = t_{14,(0,1)} = t_{14,(0,-1)}$	-0.1141 - 0.3479i (-0.0916 - 0.2868i)
$t_{13,(-1,0)} = t_{13,(-1,1)}^* = \epsilon^* t_{13,(1,-2)}^* = \epsilon^* t_{13,(1,1)} = \epsilon t_{13,(2,-2)} = \epsilon t_{13,(2,0)}^*$	-0.0034 - 0.0007i (0.0299 - 0.0279i)
$t_{14,(-1,0)} = t_{14,(-1,1)} = t_{14,(1,-2)} = t_{14,(1,1)} = t_{14,(2,-2)} = t_{14,(2,0)}$	0.0464 + 0.0831i (0.0339 + 0.0222i)
$t_{13,(-1,-1)} = \epsilon t_{13,(3,-2)} = \epsilon^* t_{13,(0,2)} = t_{13,(-1,2)}^* = \epsilon^* t_{13,(0,-2)}^* = \epsilon t_{13,(3,-1)}^*$	-0.0012 - 0.0007i (-0.0293 + 0.0009i)
$t_{14,(-1,-1)} = t_{14,(-1,2)} = t_{14,(0,-2)} = t_{14,(0,2)} = t_{14,(3,-2)} = t_{14,(3,-1)}$	-0.0179 - 0.0182i (-0.0089 + 0.0112i)
$t_{13,(-2,1)} = \epsilon t_{13,(2,-3)} = \epsilon^* t_{13,(2,1)}$	-0.0005 (0.0280)
$t_{14,(-2,1)} = t_{14,(2,-3)} = t_{14,(2,1)}$	0.0163 + 0.0213i (0.0021 - 0.0101i)
$t_{13,(-2,0)} = \epsilon t_{13,(3,-3)} = \epsilon^* t_{13,(1,2)} = t_{13,(-2,2)}^* = \epsilon^* t_{13,(1,-3)}^* = \epsilon t_{13,(3,0)}^*$	-0.0014 - 0.0006i (0.0040 + 0.0256i)
$t_{14,(-2,0)} = t_{14,(-2,2)} = t_{14,(1,-3)} = t_{14,(1,2)} = t_{14,(3,-3)} = t_{14,(3,0)}$	0.0111 + 0.0310i (0.0131 + 0.0345i)
$t_{13,(4,-2)} = \epsilon t_{13,(-1,3)} = \epsilon^* t_{13,(-1,-2)}$	0.0002(-0.0359)
$t_{14,(4,-2)} = t_{14,(-1,3)} = t_{14,(-1,-2)}$	-0.0145 - 0.0272i (-0.0154 - 0.0398i)
$t_{13,(-2,-1)} = \epsilon t_{13,(4,-3)} = \epsilon^* t_{13,(0,3)} = t_{13,(-2,3)}^* = \epsilon^* t_{13,(0,-3)}^* = \epsilon t_{13,(4,-1)}^*$	0.0005 - 0.0004i (-0.0107 - 0.0040i)
$t_{14,(-2,-1)} = t_{14,(4,-3)} = t_{14,(0,3)} = t_{14,(-2,3)} = t_{14,(0,-3)} = t_{14,(4,-1)}$	0.0081i (0.0012 + 0.0099i)

TABLE II. The hopping constants among  $w_{1,2}$  themselves and  $w_{3,4}$  themselves. The number outside (inside) the parentheses is for WSs obtained from the projection method (WANNIER90). All the numbers are in units of milli-electron volts.

$t_{11,(1,0)} = t_{11,(-1,1)} = t_{11,(0,-1)} = t_{33,(1,0)} = t_{33,(-1,1)} = t_{33,(0,-1)}$	$-0.0023 - 0.0093i$ ( $-0.0023 - 0.0161i$ )
$t_{12,(1,0)} = \epsilon t_{12,(-1,1)} = \epsilon^* t_{12,(0,-1)} = t_{34,(-1,1)} = \epsilon t_{34,(1,0)} = \epsilon^* t_{34,(0,-1)}$	$-0.0017 - 0.0038i$ ( $-0.0947 - 0.0663i$ )
$t_{11,(-2,1)} = t_{11,(1,-2)} = t_{11,(1,1)} = t_{33,(-2,1)} = t_{33,(1,-2)} = t_{33,(1,1)}$	$0.0130 - 0.0599i$ ( $0.0131 - 0.0914i$ )
$t_{12,(-2,1)} = \epsilon t_{12,(1,-2)} = \epsilon^* t_{12,(1,1)} = t_{34,(-2,1)} = \epsilon^* t_{34,(1,-2)} = \epsilon t_{34,(1,1)}$	$0.0022 - 0.0018i$ ( $0.0706 - 0.0004i$ )
$t_{11,(2,0)} = t_{11,(-2,2)} = t_{11,(0,-2)} = t_{33,(2,0)} = t_{33,(-2,2)} = t_{33,(0,-2)}$	$-0.0005 - 0.0135i$ ( $-0.0005 - 0.0182i$ )
$t_{12,(2,0)} = \epsilon t_{12,(-2,2)} = \epsilon^* t_{12,(0,-2)} = t_{34,(-2,2)} = \epsilon^* t_{34,(0,-2)} = \epsilon t_{34,(2,0)}$	$0.0007 - 0.0017i$ ( $-0.0181 + 0.0081i$ )
$t_{11,(-3,1)} = t_{11,(2,-3)} = t_{11,(1,2)} = t_{33,(3,-2)} = t_{33,(-1,3)} = t_{33,(-2,-1)}$	$0.0204 - 0.0153i$ ( $0.0302 - 0.0057i$ )
$t_{12,(-3,1)} = \epsilon t_{12,(2,-3)} = \epsilon^* t_{12,(1,2)} = t_{34,(3,-2)} = \epsilon^* t_{34,(-1,3)} = \epsilon t_{34,(-2,-1)}$	$0.0013 - 0.0011i$ ( $0.0013 + 0.0139i$ )
$t_{11,(-3,2)} = t_{11,(1,-3)} = t_{11,(2,1)} = t_{33,(3,-1)} = t_{33,(-2,3)} = t_{33,(-1,-2)}$	$-0.0139 - 0.0232i$ ( $-0.0237 - 0.0097i$ )
$t_{12,(-3,2)} = \epsilon t_{12,(1,-3)} = \epsilon^* t_{12,(2,1)} = t_{34,(3,-1)} = \epsilon^* t_{34,(-2,3)} = \epsilon t_{34,(-1,-2)}$	$0.0002 + 0.0004i$ ( $0.0016 - 0.0018i$ )
$t_{11,(3,0)} = t_{11,(-3,3)} = t_{11,(0,-3)} = t_{33,(-3,3)} = t_{33,(0,-3)} = t_{33,(3,0)}$	$0.0033 - 0.0035i$ ( $0.0033 - 0.0033i$ )
$t_{12,(3,0)} = \epsilon t_{12,(-3,3)} = \epsilon^* t_{12,(0,-3)} = t_{34,(-3,3)} = \epsilon^* t_{34,(0,-3)} = \epsilon t_{34,(3,0)}$	$0.0007 - 0.0008i$ ( $-0.0007 + 0.0073i$ )

and the lattice vector  $\mathbf{r}$ . The numerical value of the hopping constant can be obtained from the energy of the Bloch states and the transformation between the WS and the Bloch states. Suppose that

$$|w_{i,\mathbf{R}}\rangle = \int \frac{d^d \mathbf{k}}{(2\pi)^d} |\psi_{j,\mathbf{k}}\rangle e^{-i\mathbf{k}\cdot\mathbf{R}} U_{ji}(\mathbf{k}), \quad (18)$$

then

$$\begin{aligned} t_{ij,\mathbf{r}} &= \langle w_{i,\mathbf{R}} | H | w_{j,\mathbf{R}+\mathbf{r}} \rangle \\ &= \int \frac{d^d \mathbf{k} d^d \mathbf{k}'}{(2\pi)^{2d}} e^{i\mathbf{k}'\cdot\mathbf{R}} U_{i'i}^*(\mathbf{k}') \langle \psi_{i'}(\mathbf{k}') | H | \psi_{j'}(\mathbf{k}) \rangle \\ &\quad \times e^{-i\mathbf{k}\cdot(\mathbf{R}+\mathbf{r})} U_{j'j}(\mathbf{k}) \\ &= \int \frac{d^d \mathbf{k}}{(2\pi)^d} U_{i'i}^*(\mathbf{k}) \epsilon_{i'}(\mathbf{k}) U_{j'j}(\mathbf{k}) e^{-i\mathbf{k}\cdot\mathbf{r}}. \end{aligned} \quad (19)$$

In this subsection, we list the values of the hopping constants up to  $|\mathbf{r}| = 3|\mathbf{L}_1|$ . For notation convenience, we parametrize  $\mathbf{r}$  as two numbers  $(a, b)$ , where  $\mathbf{r} = a\mathbf{L}_1 + b\mathbf{L}_2$ . Note that the TRS transforms  $w_1 \leftrightarrow w_2$ , and  $w_3 \leftrightarrow w_4$ . Thus, it enforces several constraints, e.g.,  $t_{12,\mathbf{r}} = t_{21,\mathbf{r}}^*$ ,  $t_{13,\mathbf{r}} = t_{24,\mathbf{r}}^*$ , etc. In Tables I and II, for notation simplicity, we list only part of the hopping constants; the others can be obtained from the constraints due to Hermiticity of the Hamiltonian and the TRS.

We separate the hopping constants into two different tables. Table I is for the hoppings between  $w_{1,2}$  and  $w_{3,4}$ , and Table II is for the hoppings among  $w_{1,2}$  themselves and  $w_{3,4}$  themselves. For comparison, two different hopping amplitudes are listed in each row. The first one is for the WSs obtained from the projection method. As we can see, the hoppings between two WSs with different  $C_3$  eigenvalues are significantly smaller than those between two WSs from the same valley. This hierarchy of the hopping amplitudes emerges as the consequence of the approximate

valley  $U(1)$  symmetry. The numbers in the parentheses are the hopping amplitudes for the maximally localized WSs obtained from WANNIER90. We find that the hierarchy of hopping amplitudes is lost after applying the WANNIER90 procedure, suggesting that despite enforcing the exact symmetries, the WANNIER90 algorithm strongly mixes the valleys. Because of this mixing, we choose the WSs obtained from the projection method to compare our tight-binding model with the DFT result.

Figure 4 illustrates the comparison of the narrow bands obtained from the microscopic model in Ref. [20] and the tight-binding model with different hopping range  $L_c$  based on the localized WSs obtained from the projection method. For small  $L_c$ , most features of the band structure can be reproduced by our tight-binding model, except the peaks and troughs around  $\Gamma$ .

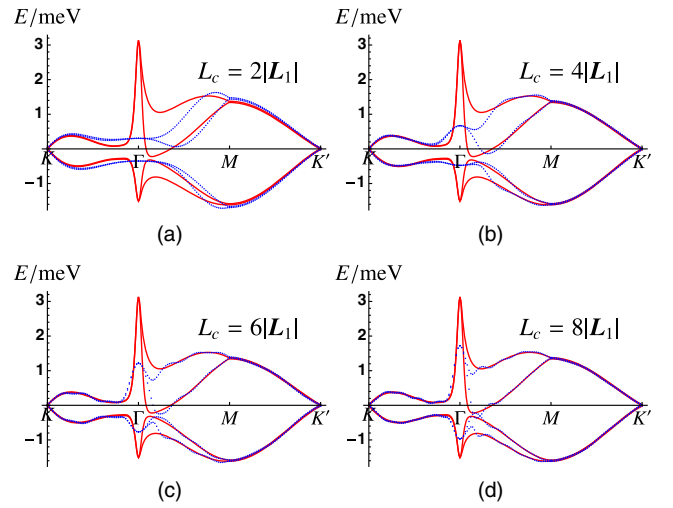


FIG. 4. Comparison of the narrow-band structure produced by the model given by Ref. [20] (red solid line) and the tight-binding model based on the WSs (blue dots) with the range of hopping (a)  $L_c = 2L$ , (b)  $L_c = 4L$ , (c)  $L_c = 6L$ , and (d)  $L_c = 8L$ .



## V. DISCUSSION

In this work, we construct the localized WSs based on the lattice model with the AA stacking configuration. Although the approximate valley  $U(1)$  symmetry is not explicitly implemented at the beginning, it is manifested in our four-band model, as shown by the Fourier transform of the WSs and the hierarchy of the hopping amplitudes. After the original version of this paper appeared on arXiv, we noticed that very similar WSs have also been constructed in Ref. [25] starting from a continuum model with valley  $U(1)$  symmetry and particle-hole symmetry explicitly present. Just as in our work, the same spatial symmetry group  $D_3$  and TRS are locally realized by the WSs, as well as the corresponding tight-binding model. As a result of the  $U(1)$  symmetry, the tight-binding model of Ref. [25] contains no hopping amplitudes between WSs with different eigenvalues of  $C_3$ . In addition, hopping amplitudes violating particle-hole symmetry are absent. In the microscopic tight-binding model we study, valley  $U(1)$  symmetry is not exact, and, therefore, small hopping amplitudes between different  $C_3$  eigenvalues are present (see Tables I and II). Similarly, the particle-hole symmetry is also violated in the microscopic model and, therefore, not present in the tight-binding model derived from our WSs.

In conclusion, we present a method for constructing symmetry-adapted maximally localized Wannier functions and the corresponding low-energy model for the four narrow bands of the TBG near the magic angle. The WSs have three peaks around the moiré triangular lattice sites but are centered at the dual honeycomb lattice sites. They form nontrivial representations of the site symmetry group. Our model provides a firm basis for further study of the many-body effects.

## ACKNOWLEDGMENTS

We thank Yuan Cao, Valla Fatemi, Liang Fu, Pablo Jarillo-Herrero, Leonid Levitov, Senthil Todardi, Ashvin Vishwanath, and Y. Y. Zhao for fruitful discussions. J. K. is supported by the National High Magnetic Field Laboratory through National Science Foundation Grant No. DMR-1157490 and the State of Florida. O. V. is supported by National Science Foundation Grant No. DMR-1506756.

- [1] Y. Cao, V. Fatemi, A. Demir, S. Fang, S. L. Tomarken, J. Y. Luo, J. D. Sanchez-Yamagishi, K. Watanabe, T. Taniguchi, E. Kaxiras, R. C. Ashoori, and P. Jarillo-Herrero, *Unconventional Superconductivity in Magic-Angle Graphene Superlattices*, *Nature (London)* **556**, 43 (2018).
- [2] Y. Cao, V. Fatemi, S. Fang, K. Watanabe, T. Taniguchi, E. Kaxiras, and P. Jarillo-Herrero, *Correlated Insulator Behaviour at Half-Filling in Magic-Angle Graphene Superlattices*, *Nature (London)* **556**, 80 (2018).

- [3] D. K. Efimkin and A. H. MacDonald, *Helical Network Model for Twisted Bilayer Graphene*, *Phys. Rev. B* **98**, 035404 (2018).
- [4] C. Xu and L. Balents, *Topological Superconductivity in Twisted Multilayer Graphene*, *Phys. Rev. Lett.* **121**, 087001 (2018).
- [5] N. F. Q. Yuan and L. Fu, *Model for Metal-Insulator Transition in Graphene Superlattices and Beyond*, *Phys. Rev. B* **98**, 045103 (2018).
- [6] H. C. Po, L. Zou, A. Vishwanath, and T. Senthil, *Origin of Mott Insulating Behavior and Superconductivity in Twisted Bilayer Graphene*, *arXiv:1803.09742*.
- [7] B. Roy and V. Juricic, *Unconventional Superconductivity in Nearly Flat Bands in Twisted Bilayer Graphene*, *arXiv:1803.11190*.
- [8] H. Guo, X. Zhu, S. Feng, and R. T. Scalettar, *Pairing Symmetry of Interacting Fermions on Twisted Bilayer Graphene Superlattice*, *Phys. Rev. B* **97**, 235453 (2018).
- [9] G. Baskaran, *Theory of Emergent Josephson Lattice in Neutral Twisted Bilayer Graphene (Moiré is Different)*, *arXiv:1804.00627*.
- [10] B. Padhi, C. Setty, and P. W. Phillips, *Doped Twisted Bilayer Graphene near Magic Angles: Proximity to Wigner Crystallization not Mott Insulation*, *arXiv:1804.01101*.
- [11] J. F. Dodaro, S. A. Kivelson, Y. Schattner, X.-Q. Sun, and C. Wang, *Phases of a Phenomenological Model of Twisted Bilayer Graphene*, *Phys. Rev. B* **98**, 075154 (2018).
- [12] T. Huang, L. Zhang, and T. Ma, *Antiferromagnetically Ordered Mott Insulator and  $d + id$  Superconductivity in Twisted Bilayer Graphene: A Quantum Monte Carlo Study*, *arXiv:1804.06096*.
- [13] L. Zhang, *Low-Energy Moiré Band Formed by Dirac Zero Modes in Twisted Bilayer Graphene*, *arXiv:1804.09047*.
- [14] S. Ray and T. Das, *Wannier Pairs in the Superconducting Twisted Bilayer Graphene and Related Systems*, *arXiv:1804.09674*.
- [15] C.-C. Liu, L.-D. Zhang, W.-Q. Chen, and F. Yang, *Chiral SDW and  $d + id$  Superconductivity in the Magic-Angle Twisted Bilayer-Graphene*, *arXiv:1804.10009*.
- [16] X. Y. Xu, K. T. Law, and P. A. Lee, *Kekulé Valence Bond Order in an Extended Hubbard Model on the Honeycomb Lattice, with Possible Applications to Twisted Bilayer Graphene*, *arXiv:1805.00478*.
- [17] T. J. Peltonen, R. Ojajärvi, and T. T. Heikkilä, *Mean-Field Theory for Superconductivity in Twisted Bilayer Graphene*, *arXiv:1805.01039*.
- [18] M. Fidrysiak, M. Zegrodnik, and J. Spałek, *Unconventional Topological Superconductivity and Phase Diagram for a Two-Orbital Model of Twisted Bilayer Graphene*, *Phys. Rev. B*, **98**, 085436 (2018).
- [19] E. J. Mele, *Commensuration and Interlayer Coherence in Twisted Bilayer Graphene*, *Phys. Rev. B* **81**, 161405(R) (2010).
- [20] P. Moon and M. Koshino, *Energy Spectrum and Quantum Hall Effect in Twisted Bilayer Graphene*, *Phys. Rev. B* **85**, 195458 (2012).
- [21] N. Marzari and D. Vanderbilt, *Maximally Localized Generalized Wannier Functions for Composite Energy Bands*, *Phys. Rev. B* **56**, 12847 (1997); N. Marzari, A. A. Mostofi, J. R. Yates, I. Souza, and D. Vanderbilt, *Maximally Local-*



- ized Wannier Functions: Theory and Applications*, [Rev. Mod. Phys.](#) **84**, 1419 (2012).
- [22] R. Sakuma, *Symmetry-Adapted Wannier Functions in the Maximal Localization Procedure*, [Phys. Rev. B](#) **87**, 235109 (2013).
- [23] L. D. Landau and E. M. Lifshitz, *Quantum Mechanics, Course of Theoretical Physics*, 3rd ed. (Pergamon, New York, 1999), Vol. 3, p. 379.
- [24] A. A. Mostofi, J. R. Yates, G. Pizzi, Y.-S. Lee, I. Souza, D. Vanderbilt, and N. Marzari, *WANNIER90: A Tool for Obtaining Maximally-Localised Wannier Functions*, [Comput. Phys. Commun.](#) **185**, 2309 (2014).
- [25] M. Koshino, N. F. Q. Yuan, T. Koretsune, M. Ochi, K. Kuroki, and L. Fu, preceding paper, *Maximally Localized Wannier Orbitals and the Extended Hubbard Model for Twisted Bilayer Graphene*, [Phys. Rev. X](#) **8**, 031087 (2018).